Cumhuriyet Science Journal
CSJ

e-ISSN: 2587-246X
ISSN: 2587-2680

Cumhuriyet Sci. J., Vol.39-4(2018) 1107-1117

Fast Solutions for Lossless Anisotropic Electromagnetic Scattering and Radiation Problems Using the FDTD Method

Fatih KABURCUK

Erzurum Technical University, Electrical-Electronics Engineering Department, Erzurum, TURKEY

Received: 12.02.2018; Accepted: 17.10.2018 *http://dx.doi.org/10.17776/csj.393743*

Abstract. In this paper, an acceleration technique is proposed to solve electromagnetic scattering and radiation problems, which contain lossless anisotropic (Lossless-ANI) materials, based on the finite-difference time-domain (FDTD) method. This technique provides a remarkable reduction in the simulation time of Lossless-ANI electromagnetic problems. A microstrip patch antenna (MPA) with a Lossless-ANI substrate, and electromagnetic scattering and radiation problems involved a Lossless-ANI scattering object are analyzed to show the performance of the acceleration technique. Numerical results show that resonant frequencies of the MPA, the bistatic radar cross section (RCS) of the scattering problem, and the directivity pattern of the radiation problem are affected by the anisotropy.

Keywords: Electromagnetic scattering and radiation, finite-difference time-domain (FDTD) method, anisotropic material.

Kayıpsız Eşyönsüz Elektromanyetik Saçılma ve Işıma Problemlerini Sonlu Farklar Zaman Uzayı Yöntemini Kullanarak Hızlı Çözümler

Özet. Bu makalede, sonlu farklar zaman uzayı (FDTD) yöntemine dayanan kayıpsız eşyönsüz materyeller içeren elektromanyetik saçılma ve ışıma problemlerini çözmek için bir hızlandırma tekniği önerilmiştir. Bu teknik sayesinde kayıpsız eşyönsüz elektromanyetik problemlerin simulasyon süreleri önemli derecede azalmaktadır. Hızlandırma tekniğinin performansını göstermek için kayıpsız eşyönsüz alttaş üzerine mikroşerit anten ve kayıpsız eşyönsüz nesne içeren elektromanyetik saçılma ve ışıma problemlerinin analizi yapılmıştır. Sonuç olarak, mikroşerit antenin rezonans frekansları, saçılma probleminin radar kesit alanı ve ışıma probleminin yönlülük örüntüsü eşyönsüzlükten etkilenmektedir.

Anahtar Kelimeler: Elektromanyetik saçılma ve ışıma, sonlu farklar zaman uzayı yöntemi, eşyönsüz malzeme.

1. INTRODUCTION

Lossless anisotropic (Lossless-ANI) materials are materials whose permittivity and permeability are functions of the vector direction of the electric and magnetic fields, respectively, whereas the permittivity and permeability of the isotropic materials are the same in all directions. Directionally dependent permittivity and permeability affect significantly the electromagnetic behavior of the materials because the relationships between the electric field (E) and the electric flux density (D), and between the magnetic field (H) and magnetic flux density (B) are nonlinear. This nonlinearity between the fields increases the complexity of the formulation and the simulation time of the electromagnetic scattering and radiation problems involved anisotropic materials.

---

* Corresponding author. *Email address: fatih.kaburcuk@erzurum.edu.tr*

The finite difference time domain (FDTD) method is one of the most popular and useful numerical methods for solving the electromagnetic scattering and radiation problems involving isotropic, dispersive, and anisotropic materials. The lossy anisotropic algorithm based on the FDTD method was proposed in [1-5] for solving the lossy anisotropic scattering and radiation problems. The lossless anisotropic (Lossless-ANI) algorithm based on the FDTD method was first proposed in [6] for solving a microstrip patch antenna (MPA) on a Lossless-ANI substrate with permittivity tensor, and then extended in [7] for the Lossless-ANI materials with permittivity and permeability tensors. The FDTD method for solving Lossless-ANI material requires large computer memory and long simulation time. Therefore, an acceleration technique proposed here is applied to the MPA on a Lossless-ANI substrate, the Lossless-ANI scattering, and radiation problems to reduce the required computer memory and simulation time. This technique is based on dividing the problem domains into two sub-regions: one is free-space region, and the other is the anisotropic region involved an anisotropic object. In the free-space region, the isotropic formulation based on the FDTD method is performed, whereas the Lossless-ANI formulation based on the FDTD method is applied to only anisotropic region instead of applying to the entire problem domain. Therefore, this technique provides a significant reduction in the simulation time of the Lossless-ANI scattering and radiation problems.

In this paper, details of the Lossless-ANI algorithm and acceleration technique are presented in Section 2. The Lossless-ANI scattering and radiation problems are analyzed to verify the performance of the acceleration technique in Section 3. Numerical results are presented in Section 4.

2. LOSSLESS ANISOTROPIC ALGORITHM BASED ON FDTD METHOD

In this section, the formulation of the Lossless-ANI algorithm based on the FDTD method are presented for the dielectric and magnetic anisotropic materials. In Lossless-ANI material, the *D* field is related to the *E* fields by a permittivity tensor ($\bar{\bar{\varepsilon}}$) and the *B* field is related to the *H* fields by a permeability tensor ($\bar{\bar{\mu}}$). These tensors have nine unique elements.

$$\begin{bmatrix} D_x \\ D_y \\ D_z \end{bmatrix} = \bar{\bar{\varepsilon}} \begin{bmatrix} E_x \\ E_y \\ E_z \end{bmatrix} = \varepsilon_0 \begin{bmatrix} \varepsilon_{xx} & \varepsilon_{xy} & \varepsilon_{xz} \\ \varepsilon_{yx} & \varepsilon_{yy} & \varepsilon_{yz} \\ \varepsilon_{zx} & \varepsilon_{zy} & \varepsilon_{zz} \end{bmatrix} \begin{bmatrix} E_x \\ E_y \\ E_z \end{bmatrix} \text{ and } \begin{bmatrix} B_x \\ B_y \\ B_z \end{bmatrix} = \bar{\bar{\mu}} \begin{bmatrix} H_x \\ H_y \\ H_z \end{bmatrix} = \mu_0 \begin{bmatrix} \mu_{xx} & \mu_{xy} & \mu_{xz} \\ \mu_{yx} & \mu_{yy} & \mu_{yz} \\ \mu_{zx} & \mu_{zy} & \mu_{zz} \end{bmatrix} \begin{bmatrix} H_x \\ H_y \\ H_z \end{bmatrix} \quad (1)$$

The general form of Maxwell equations for Lossless-ANI material can be written the following set of four equations [6-7]:

$$\begin{gathered} \frac{\partial B}{\partial t} = -\nabla \times E \\ B = \bar{\bar{\mu}} H \quad \Longrightarrow \quad H = [\bar{\bar{\mu}}]^{-1} B \\ \frac{\partial D}{\partial t} = \nabla \times H \\ D = \bar{\bar{\varepsilon}} E \quad \Longrightarrow \quad E = [\bar{\bar{\varepsilon}}]^{-1} D \end{gathered} \quad (2)$$

where $[\bar{\bar{\varepsilon}}]^{-1}$ and $[\bar{\bar{\mu}}]^{-1}$ are the inverse of the permittivity and permeability tensors, respectively, and written as:

$$[\bar{\bar{\varepsilon}}]^{-1} = \frac{1}{\Delta_\varepsilon} \begin{bmatrix} \varepsilon'_{xx} & \varepsilon'_{xy} & \varepsilon'_{xz} \\ \varepsilon'_{yx} & \varepsilon'_{yy} & \varepsilon'_{yz} \\ \varepsilon'_{zx} & \varepsilon'_{zy} & \varepsilon'_{zz} \end{bmatrix} \text{ and } [\bar{\bar{\mu}}]^{-1} = \frac{1}{\Delta_\mu} \begin{bmatrix} \mu'_{xx} & \mu'_{xy} & \mu'_{xz} \\ \mu'_{yx} & \mu'_{yy} & \mu'_{yz} \\ \mu'_{zx} & \mu'_{zy} & \mu'_{zz} \end{bmatrix} \quad (3)$$

where

$$\begin{gathered}
\varepsilon'_{xx} = \varepsilon_{yy}\varepsilon_{zz} - \varepsilon_{yz}\varepsilon_{zy}\,,\ \varepsilon'_{xy} = \varepsilon_{xz}\varepsilon_{zy} - \varepsilon_{xy}\varepsilon_{zz}\,,\ \varepsilon'_{xz} = \varepsilon_{xy}\varepsilon_{yz} - \varepsilon_{xz}\varepsilon_{yy} \\
\varepsilon'_{yx} = \varepsilon_{yz}\varepsilon_{zx} - \varepsilon_{yx}\varepsilon_{zz}\,,\ \varepsilon'_{yy} = \varepsilon_{xx}\varepsilon_{zz} - \varepsilon_{xz}\varepsilon_{zx}\,,\ \varepsilon'_{yz} = \varepsilon_{xz}\varepsilon_{yx} - \varepsilon_{xx}\varepsilon_{yz} \\
\varepsilon'_{zx} = \varepsilon_{yx}\varepsilon_{zy} - \varepsilon_{yy}\varepsilon_{zx}\,,\ \varepsilon'_{zy} = \varepsilon_{xy}\varepsilon_{zx} - \varepsilon_{xx}\varepsilon_{zy}\,,\ \varepsilon'_{zz} = \varepsilon_{xx}\varepsilon_{yy} - \varepsilon_{xy}\varepsilon_{yx} \\
\mu'_{xx} = \mu_{yy}\mu_{zz} - \mu_{yz}\mu_{zy}\,,\ \mu'_{xy} = \mu_{xz}\mu_{zy} - \mu_{xy}\mu_{zz}\,,\ \mu'_{xz} = \mu_{xy}\mu_{yz} - \mu_{xz}\mu_{yy} \\
\mu'_{yx} = \mu_{yz}\mu_{zx} - \mu_{yx}\mu_{zz}\,,\ \mu'_{yy} = \mu_{xx}\mu_{zz} - \mu_{xz}\mu_{zx}\,,\ \mu'_{yz} = \mu_{xz}\mu_{yx} - \mu_{xx}\mu_{yz} \\
\mu'_{zx} = \mu_{yx}\mu_{zy} - \mu_{yy}\mu_{zx}\,,\ \mu'_{zy} = \mu_{xy}\mu_{zx} - \mu_{xx}\mu_{zy}\,,\ \mu'_{zz} = \mu_{xx}\mu_{yy} - \mu_{xy}\mu_{yx}
\end{gathered} \tag{4}$$

$$\begin{gathered}
\Delta_\varepsilon = \varepsilon_0 \begin{pmatrix} \varepsilon_{xx}\varepsilon_{yy}\varepsilon_{zz} + \varepsilon_{xy}\varepsilon_{yz}\varepsilon_{zx} + \varepsilon_{xz}\varepsilon_{yx}\varepsilon_{zy} \\ -\varepsilon_{xz}\varepsilon_{yy}\varepsilon_{zx} - \varepsilon_{xy}\varepsilon_{yx}\varepsilon_{zz} - \varepsilon_{xx}\varepsilon_{yz}\varepsilon_{zy} \end{pmatrix} \\
\Delta_\mu = \mu_0 \begin{pmatrix} \mu_{xx}\mu_{yy}\mu_{zz} + \mu_{xy}\mu_{yz}\mu_{zx} + \mu_{xz}\mu_{yx}\mu_{zy} \\ -\mu_{xz}\mu_{yy}\mu_{zx} - \mu_{xy}\mu_{yx}\mu_{zz} - \mu_{xx}\mu_{yz}\mu_{zy} \end{pmatrix}
\end{gathered} \tag{5}$$

The Lossless-ANI algorithm is based on updating the *D*, *E*, *B*, and *H* fields using four equations in (2). These four equations are updated in order: beginning with *E* fields, then updating *B* fields from *E* fields. Then *H* fields are updated from *B* fields after the convolution perfectly matched layers (CPML) is applied to *B* fields. *D* fields are updated from *H* fields, then CPML is applied to *D* fields. Finally, *E* fields are updated from *D* fields.

The updated *E* fields obtained from *D* fields in (2) are written in the following form at the time step *n* with the proper discretized spatial coordinates:

$$E_x\Big|_{i-0.5,j,k}^{n+1} = \frac{\varepsilon'_{xx}}{\Delta_\varepsilon} D_x\Big|_{i-0.5,j,k}^{n+1} + \frac{\varepsilon'_{xy}}{\Delta_\varepsilon} D_y\Big|_{i-0.5,j,k}^{n+1} + \frac{\varepsilon'_{xz}}{\Delta_\varepsilon} D_z\Big|_{i-0.5,j,k}^{n+1} \tag{6.a}$$

$$E_y\Big|_{i,j-0.5,k}^{n+1} = \frac{\varepsilon'_{yx}}{\Delta_\varepsilon} D_x\Big|_{i,j-0.5,k}^{n+1} + \frac{\varepsilon'_{yy}}{\Delta_\varepsilon} D_y\Big|_{i,j-0.5,k}^{n+1} + \frac{\varepsilon'_{yz}}{\Delta_\varepsilon} D_y\Big|_{i,j-0.5,k}^{n+1} \tag{6.b}$$

$$E_z\Big|_{i,j,k-0.5}^{n+1} = \frac{\varepsilon'_{zx}}{\Delta_\varepsilon} D_x\Big|_{i,j,k-0.5}^{n+1} + \frac{\varepsilon'_{zy}}{\Delta_\varepsilon} D_y\Big|_{i,j,k-0.5}^{n+1} + \frac{\varepsilon'_{zz}}{\Delta_\varepsilon} D_z\Big|_{i,j,k-0.5}^{n+1} \tag{6.c}$$

It can be noticed that the D_y and D_z field components in (6.a) do not fit in the FDTD cells and an average over four points surrounding the desired locations in the FDTD cells is calculated such that:

$$D_y^n(i,j,k) = \frac{1}{4}\left[D_y^n(i+1,j+1,k) + D_y^n(i+1,j,k) + D_y^n(i,j+1,k) + D_y^n(i,j,k)\right] \tag{7.a}$$

$$D_z^n(i,j,k) = \frac{1}{4}[D_z^n(i+1,j,k+1) + D_z^n(i+1,j,k) + D_z^n(i,j,k+1) + D_z^n(i,j,k)] \tag{7.b}$$

Similarly, same modifications are made for D_x and D_z in (6.b), D_x and D_y in (6.c).

The updated *H* fields obtained from *B* fields in (2) are written in the following form at the time step *n* with the proper discretized spatial coordinates:

$$H_x\Big|_{i,j-0.5,k-0.5}^{n+0.5} = \frac{\mu'_{xx}}{\Delta_\mu} B_x\Big|_{i,j-0.5,k-0.5}^{n+0.5} + \frac{\mu'_{xy}}{\Delta_\mu} B_y\Big|_{i,j-0.5,k-0.5}^{n+0.5} + \frac{\mu'_{xz}}{\Delta_\mu} B_z\Big|_{i,j-0.5,k-0.5}^{n+0.5} \tag{8.a}$$

$$H_y\Big|_{i-0.5,j,k-0.5}^{n+0.5} = \frac{\mu'_{yx}}{\Delta_\mu} B_x\Big|_{i-0.5,j,k-0.5}^{n+0.5} + \frac{\mu'_{yy}}{\Delta_\mu} B_y\Big|_{i-0.5,j,k-0.5}^{n+0.5} + \frac{\mu'_{yz}}{\Delta_\mu} B_z\Big|_{i-0.5,j,k-0.5}^{n+0.5} \tag{8.b}$$

$$H_z\Big|_{i-0.5,j-0.5,k}^{n+0.5} = \frac{\mu'_{zx}}{\Delta_\mu} B_x\Big|_{i-0.5,j-0.5,k}^{n+0.5} + \frac{\mu'_{zy}}{\Delta_\mu} B_y\Big|_{i-0.5,j-0.5,k}^{n+0.5} + \frac{\mu'_{zz}}{\Delta_\mu} B_z\Big|_{i-0.5,j-0.5,k}^{n+0.5} \tag{8.c}$$

With a similar approach, the B_y and B_z field components in (8.a) do not fit in the FDTD cells and an average over four points surrounding the desired locations in the FDTD cells is calculated such that:

$$B_y^n(i,j,k) = \frac{1}{4}\left[B_y^n(i+1,j+1,k) + B_y^n(i+1,j,k) + B_y^n(i,j+1,k) + B_y^n(i,j,k)\right] \tag{9.a}$$

$$B_z^n(i,j,k) = \frac{1}{4}\left[B_z^n(i+1,j,k+1) + B_z^n(i+1,j,k) + B_z^n(i,j,k+1) + B_z^n(i,j,k)\right] \tag{9.b}$$

Similarly, same modifications are made for B_x and B_z in (8.b), B_x and B_y in (8.c).

The tangential electric field (E_t) should be set to zero on the surface of the PEC patch on the Lossless-ANI substrate. Therefore, when a PEC plate is located at $k = k_0$ plane in Cartesian coordinates, the electric fields E_x and E_y on the PEC are being set through their coefficients in (6.a) and (6.b) equal to zero as follows:

$$\begin{aligned} \varepsilon'_{xx}(i,j,k_0) = \varepsilon'_{xy}(i,j,k_0) = \varepsilon'_{xz}(i,j,k_0) = 0 \\ \varepsilon'_{yx}(i,j,k_0) = \varepsilon'_{yy}(i,j,k_0) = \varepsilon'_{yz}(i,j,k_0) = 0 \end{aligned} \tag{10}$$

3. ACCELERATION TECHNIQUE FOR LOSSLESS-ANI ALGORITHM

The Lossless-ANI algorithm is applied to the entire FDTD problem domain which consists of the anisotropic material and free-space. It is realized that most of the simulation time is consumed by analyzing the free-space using the Lossless-ANI algorithm. In this paper, we present an acceleration technique that allows to analyze the anisotropic material using the Lossless-ANI algorithm and the free-space using the isotropic FDTD formulation [9]. In this technique, the FDTD problem domain shown in Figure 1 is considered to have two sub-regions: one is free-space region and the other is anisotropic region. In the free-space region, the isotropic FDTD formulation is performed to update *E* and *H* fields, whereas, in the anisotropic region, the Lossless-ANI algorithm is performed to update *B*, *H*, *D*, and *E* fields sequentially. Then, these fields are used to update fields in the next FDTD time-step in the simulation. This technique provides more than 50% reduction in the simulation time of the problems.

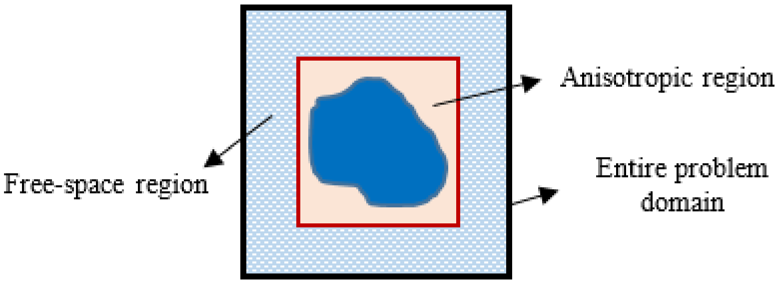

Figure 1. Configuration of the FDTD problem domain divided into the free-space and anisotropic regions.

4. NUMERICAL RESULTS

In this section, the performance of the Lossless-ANI algorithm with the acceleration technique is tested for solving an MPA [10] on a Lossless-ANI substrate, and Lossless-ANI electromagnetic scattering and radiation problems. In all simulations, a personal computer used in this work has Intel® Core™ i7-4790

CPU and 8 GB DDR RAM. The program is written and compiled in 64-bit MATLAB version 8.2.0.701 (R2013b). The convolution perfectly matched layers (CPML) [8] are used here to truncate the FDTD problem domain. The boundaries of the problems here are terminated by an 8 cells thickness CPML and 10 cells air gap is introduced between the objects in the problem and the CPML boundaries.

4.1. Electromagnetic Scattering from a Lossless-ANI Sphere

The bistatic RCS of a Lossless-ANI sphere is calculated to show the effect of the anisotropy and to verify the efficiency of the Lossless-ANI algorithm with the acceleration technique. Figure 2 shows the Lossless-ANI sphere illuminated by an *z* polarized plane wave traveling in the positive *y*-direction. A Gaussian waveform is used as an incident plane wave. The diameter of the Lossless-ANI sphere is 20 cm. The cell size of the problem space in each direction is 5 mm. The bistatic RCS of the sphere are calculated for the three plane cuts (*xy*, *xz*, and *yz*) at 1 GHz. The simulation is performed for 2000 time steps.

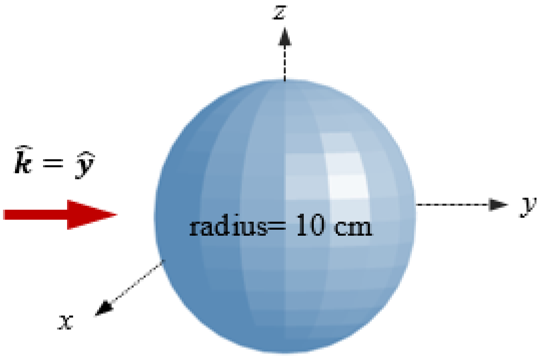

Figure 2. Geometry of the Lossless-ANI sphere.

Three different simulations for the Lossless-ANI sphere are considered in this example. In the first simulation, the material parameters of the Lossless-ANI sphere are given as follows:

$$\bar{\bar{\varepsilon}} = \varepsilon_o \begin{bmatrix} 3 & 0.9 & 0 \\ 0.9 & 3 & 0 \\ 0 & 0 & 3 \end{bmatrix} \text{ and } \bar{\bar{\mu}} = \mu_o \begin{bmatrix} 2 & 0.6 & 0 \\ 0.6 & 2 & 0 \\ 0 & 0 & 2 \end{bmatrix} \quad (11)$$

In the second simulation, the material parameters of the Lossless-ANI sphere are given as follows:

$$\bar{\bar{\varepsilon}} = \varepsilon_o \begin{bmatrix} 3 & 0 & 0.9 \\ 0 & 3 & 0 \\ 0.9 & 0 & 3 \end{bmatrix} \text{ and } \bar{\bar{\mu}} = \mu_o \begin{bmatrix} 2 & 0 & 0.6 \\ 0 & 2 & 0 \\ 0.6 & 0 & 2 \end{bmatrix} \quad (12)$$

In the third simulation, the material parameters of these Lossless-ANI sphere are given as follows:

$$\bar{\bar{\varepsilon}} = \varepsilon_o \begin{bmatrix} 3 & 0 & 0 \\ 0 & 3 & 0.9 \\ 0 & 0.9 & 3 \end{bmatrix} \text{ and } \bar{\bar{\mu}} = \mu_o \begin{bmatrix} 2 & 0 & 0 \\ 0 & 2 & 0.6 \\ 0 & 0.6 & 2 \end{bmatrix} \quad (13)$$

The bistatic RCSs for the *xy*, *xz*, and *yz* plane cuts in Figure 3 obtained from the three simulations are calculated at 1 GHz using the electromagnetic scattering fields from the Lossless-ANI sphere. These results are compared with the RCS obtained from the isotropic sphere when the material parameters are set to relative permitivity (ε_r=3) and relative permeability (μ_r=2). It can be seen from Figure 3 that the direction of the anisotropy in the sphere effects the magnitude of the RCS. The simulation time of the Lossless-ANI sphere with the acceleration technique is 5 min 43 s, whereas those without the acceleration technique is 11 min 54 s. Therefore, the acceleration technique provides 52% reduction in the simulation time.

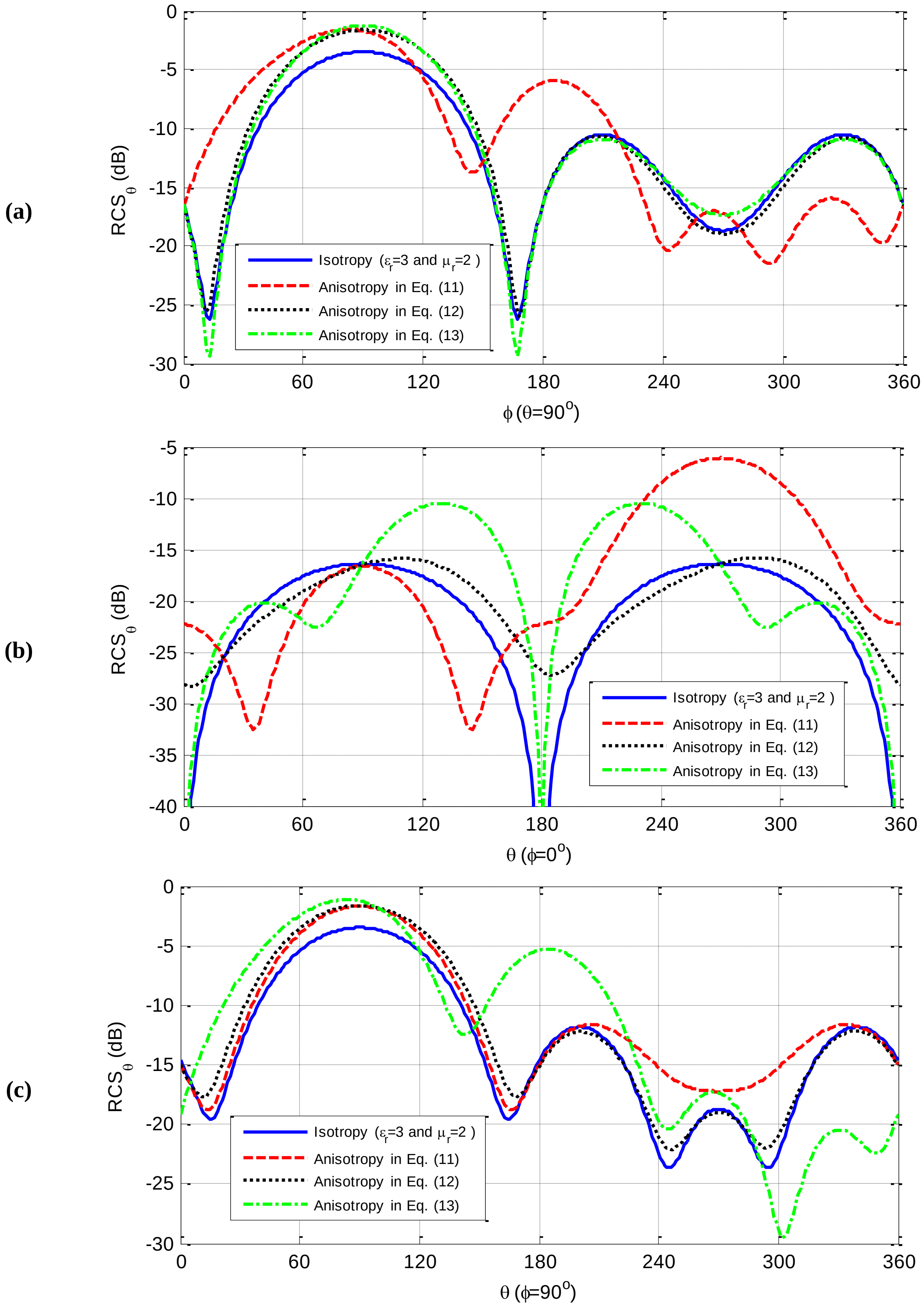

Figure 3. Bistatic RCSs for a) *xy* b) *xz* c) *yz* plane cuts.

4.2. Electromagnetic Radiation from a Dipole Antenna in the Presence of a Lossless-ANI Sphere

Figure 4 shows the problem geometry which consists of two objects: a dipole antenna placed a distance 2 cm away from a Lossless-ANI sphere along the *x*-direction. The dimensions and material properties of the sphere are the same as those of the Lossless-ANI sphere given in Figure 2. The length and radius of the dipole antenna are 16 cm and 0.25 mm, respectively. The discrization of the problem is 2 mm in all directions. The dipole antenna is excited by a voltage source with a Gaussian waveform. The single dipole antenna is simulated to determine the operating resonance frequency in which the antenna radiates well. The resonance frequency is 900 MHz and the input reflection coefficient (S_{11}) of the single dipole antenna is shown in Figure 5.

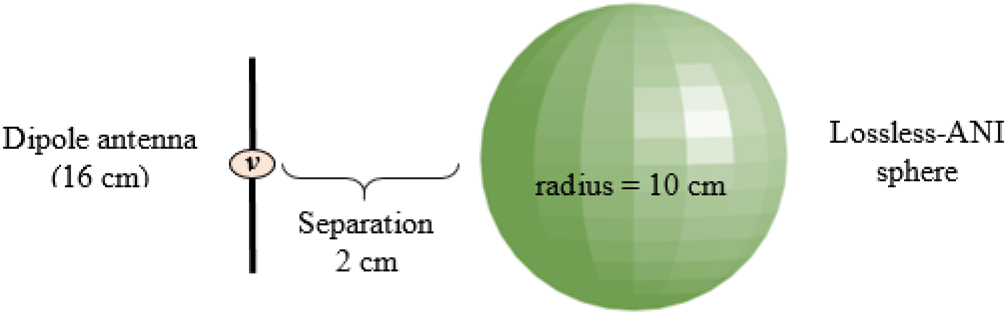

Figure 4. Geometry of a dipole antenna in the presence of a Lossless-ANI sphere.

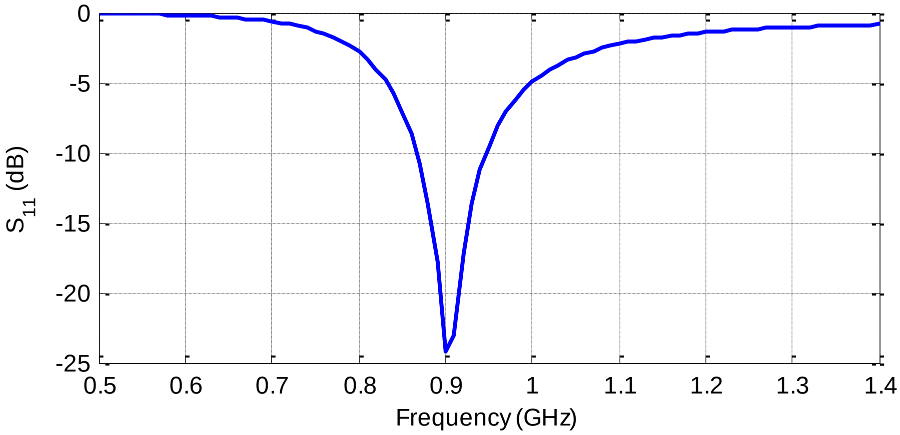

Figure 5. S_{11} of a single dipole antenna.

The simulation is performed for 4000 time steps. Three different simulations for this problem are performed when the material parameters given in (11)-(13) are used for the Lossless-ANI sphere. Since this is a radiation problem, the directivity patterns are calculated as far-field radiation patterns at 900 MHz. The directivity patterns for the three plane cuts are plotted in Figure 6 to show the direction effect of the anisotropy in the sphere. These results are compared with the directivity patterns obtained from the isotropic sphere when the material parameters are set to ε_r=3 and μ_r=2. The simulation time of the problem with the acceleration technique is 151 min, whereas those without the acceleration technique is 309 min 54 s. Therefore, the acceleration technique provides 51% reduction in the simulation time. Furthermore, considerable reduction in the simulation time can be achieved especially with larger separation between the dipole antenna and the sphere.

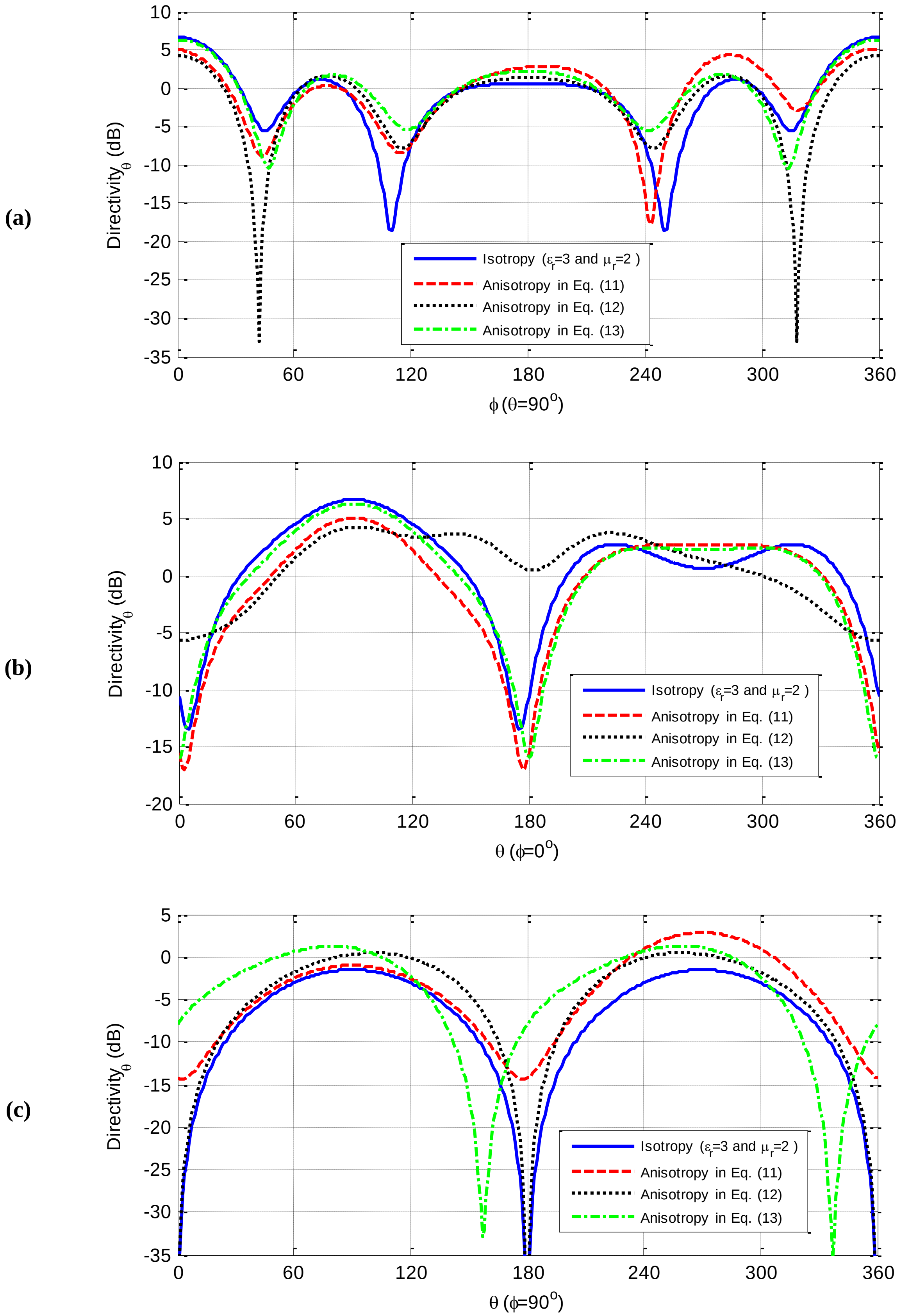

Figure 6. Directivity patterns for a) *xy* b) *xz* c) *yz* plane cuts.

4.3. Microstrip Patch Antenna with a Lossless-ANI Substrate

A microstrip patch antenna with a Lossless-ANI substrate, shown in Figure 7, is analyzed using the Lossless-ANI algorithm with the acceleration technique. The cell size of the problem is d*x*=0.3891 mm, dy=0.4 mm, and dz=0.1985 mm. The size of the rectangular patch is (31 dx)×(40 dy). The length and width of feeding line are 30dy and 6dx, respectively. The MPA is excited by a voltage source with a Gaussian waveform. The simulation is performed for 5000 time-steps.

In order to verify the result obtained using the Lossless-ANI algorithm in comparison with that obtained using the isotropic FDTD formulation, the MPA with isotropic (ε_r=2.2 and μ_r=1) substrate is solved. The input reflection coefficients (S_{11}) of the MPA, shown in Figure 8, show excellent agreement. The operating resonant frequencies of the MPA are 7.68 GHz and 18.04 GHz.

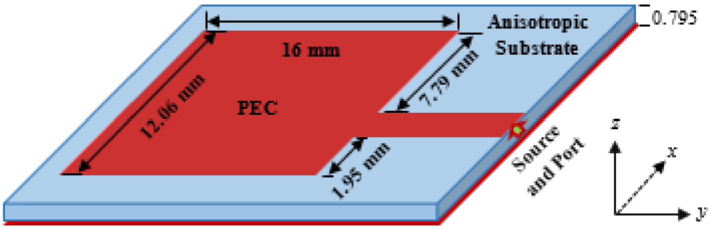

Figure 7. Configuration of the MPA with the Lossless-ANI substrate.

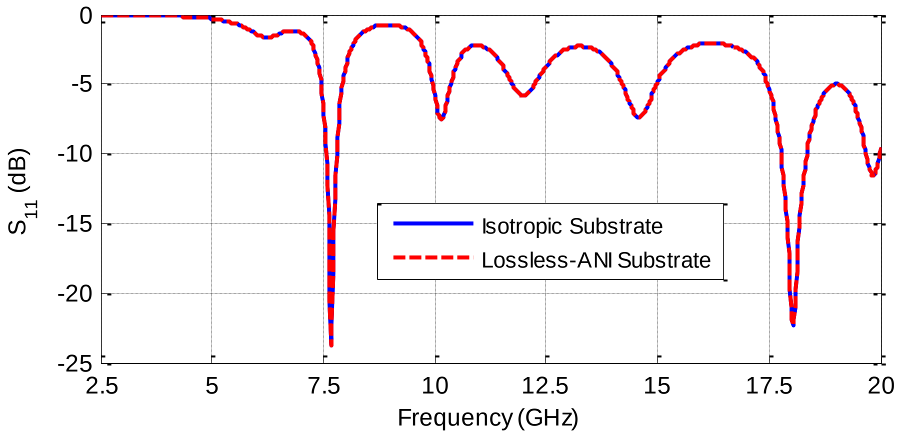

Figure 8. S_{11} of the MPA with the isotropic substrate obtained using the Lossless-ANI algorithm and the isotropic FDTD formulation.

Two different simulations for the anisotropic substrate are performed. In the first simulation, the elements of permittivity and permeability tensors for the anisotropic substrate are given as follows:

$$\begin{gathered}
\varepsilon_{xx} = \varepsilon_1 \cos^2\theta + \varepsilon_2 \sin^2\theta, \varepsilon_{yy} = \varepsilon_1, \varepsilon_{zz} = \varepsilon_1 \sin^2\theta + \varepsilon_2 \cos^2\theta \\
\varepsilon_{xz} = \varepsilon_{zx} = (\varepsilon_1 - \varepsilon_2) \sin\theta \cos\theta, \varepsilon_{xy} = \varepsilon_{yx} = \varepsilon_{yz} = \varepsilon_{zy} = 0 \\
\mu_{xx} = \mu_1 \cos^2\theta + \mu_2 \sin^2\theta, \mu_{yy} = \mu_1, \mu_{zz} = \mu_1 \sin^2\theta + \mu_2 \cos^2\theta \\
\mu_{xz} = \mu_{zx} = (\mu_1 - \mu_2) \sin\theta \cos\theta, \mu_{xy} = \mu_{yx} = \mu_{yz} = \mu_{zy} = 0
\end{gathered} \tag{14}$$

where θ is the angle between the optical axis and the *x*-direction. In the second simulation, the elements of permittivity and permeability tensors for the anisotropic substrate are given as follows:

$$\begin{gathered}
\varepsilon_{xx} = \varepsilon_1\,, \varepsilon_{yy} = \varepsilon_1 cos^2\phi + \varepsilon_2\, sin^2\phi, \varepsilon_{zz} = \varepsilon_1\, sin^2\phi + \varepsilon_2\, cos^2\phi \\
\varepsilon_{yz} = \varepsilon_{zy} = (\varepsilon_1 - \varepsilon_2)\, sin\phi\, cos\phi, \varepsilon_{xy} = \varepsilon_{yx} = \varepsilon_{xz} = \varepsilon_{xz} = 0 \\
\mu_{xx} = \mu_1\,, \mu_{yy} = \mu_1 cos^2\phi + \mu_2\, sin^2\phi, \mu_{zz} = \mu_1\, sin^2\phi + \mu_2\, cos^2\phi \\
\mu_{yz} = \mu_{zy} = (\mu_1 - \mu_2)\, sin\phi\, cos\phi, \mu_{xy} = \mu_{yx} = \mu_{xz} = \mu_{zx} = 0
\end{gathered} \tag{15}$$

where ϕ is the angle between the optical axis and the y-direction. The S_{11} as a function of θ and ϕ obtained using the Lossless-ANI algorithm are shown in Figure 9 and Figure 10, respectively, when ε_1=2.35, ε_2=2.05, μ_1=1.1, and μ_2=0.9 in (14) and (15). It can be observed from Figure 9 and Figure 10 that the resonant frequencies of the MPA are affected by the anisotropy in the substrate. It can be observed from Figure 9 that the lowest operating resonant frequency of the MPA is decreasing when the angle θ is increasing from zero to π/2, whereas the highest operating resonant frequency of the MPA is increasing. The resonant frequencies of the MPA are tabulated in Table 1 to show the effect of the angles (θ and ϕ) in the substrate. The simulation time of the MPA with the acceleration technique is 14 min 25 s, whereas those without the acceleration technique is 30 min 38 s. This presented technique provides 53% reduction in the simulation time.

Table 1. The operating resonant frequencies of the MPA versus the angles of θ and ϕ.

Angle	***θ***			***ϕ***		
	0	**π/4**	**π/2**	**0**	**π/4**	**π/2**
Lowest resonant frequency (GHz)	7.56	7.36	7.10	7.40	7.74	8.08
Highest resonant frequency (GHz)	17.80	18.10	18.40	17.44	16.90	16.38

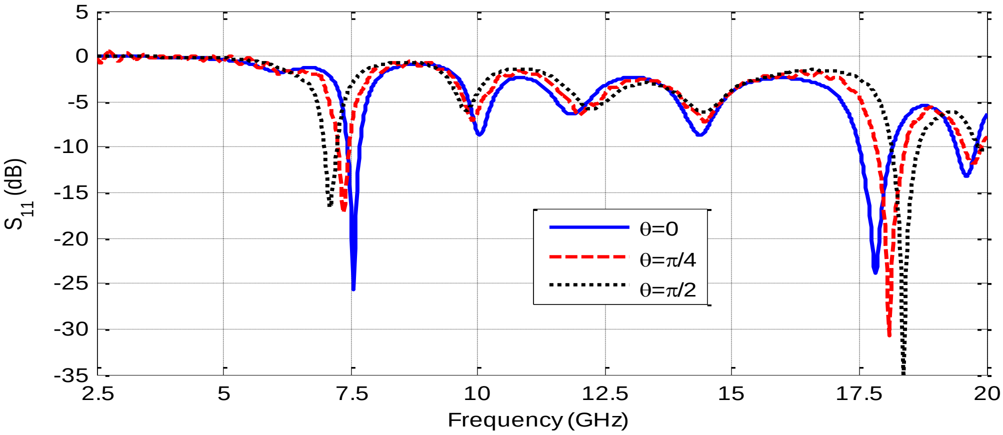

Figure 9. S_{11} of the MPA as a function of θ obtained using the Lossless-ANI algorithm.

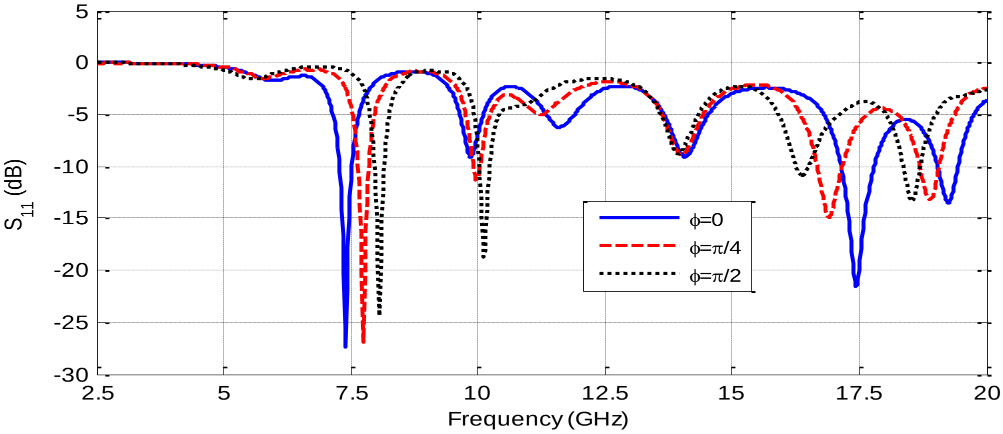

Figure 10. S_{11} of the MPA as a function of ϕ obtained using the Lossless-ANI algorithm.

5. CONCLUSION

In this paper, the performance of the acceleration technique integrated into the Lossless-ANI algorithm based on the FDTD method is presented for solving the electromagnetic scattering and radiation problems containing Lossless-ANI material. The acceleration technique provides remarkable reduction in the computation time of configurations containing Lossless-ANI material. It can be realized from the numerical results that the resonant frequencies of the MPA with the Lossless-ANI substrate, the bistatic radar cross section (RCS) of the Lossless-ANI scattering problem, and the directivity pattern of the Lossless-ANI radiation problem are affected by the direction of the anisotropy.

REFERENCES

[1] Schneider J. and Hudson S., The finite-difference time-domain method applied to anisotropic material, IEEE Trans. on Antennas and Propagation, 41-7 (1993) 994–999.

[2] Ge D., Yang L., Wei B., Ge N., and Zheng K., FDTD applied to lossy anisotropic medium and its parallel computing, Proceedings of ISAP, Seoul, Korea (2005).

[3] Jung K. Y., Teixeira F. L., and Lee R., Complex envelope PML-ADI-FDTD method for lossy anisotropic dielectrics, IEEE Antennas. Wireless Propag. Lett., 6 (2007) 643–646.

[4] Kaburcuk F. and Elsherbeni A. Z., A speeding up Technique for Lossy Anisotropic Algorithm in FDTD Method, Applied Computational Electromagnetics Society Journal, 31-12 (2016) 1377–1381.

[5] Kaburcuk F. and Elsherbeni A. Z., A speeding up technique for lossy anisotropic algorithm in FDTD method, 2017 International Applied Computational Electromagnetics Society Symposium - Italy (ACES), Florence, 2017.

[6] Zhao A. P., Juntunen J., and Raisanen A. V., An efficient FDTD algortihm for the analysis of microstrip patch antennas printed on a general anisotropic substrate, IEEE Trans. Microwave Theory Tech., 47-7 (1999) 1142-1146.

[7] Dou L. and Sebak A. R., 3D FDTD method for arbitrary anisotropic materials, Microw. Opt. Technol. Lett., 48-10 (2006) 2083–2090.

[8] Roden J. and Gedney S., Convolution PML (CPML): an efficient FDTD implementation of the CFS-PML for arbitrary media, Microwave and Optical Technology Letters, 27-5 (2000) 334–339.

[9] Elsherbeni A. Z. and Demir V., The Finite-Difference Time-Domain Method for Electromagnetics with MATLAB Simulations, 2nd ed. New Jersey: SciTech Publishing, 2016.

[10] Sheen D. M., Ali S. M., Abouzahra M. D., and Kong J. A., Application of the three-dimensional finite-difference time-domain method to the analysis of planar microstrip circuits, IEEE Trans. Microwave Theory Tech., 38-7 (1990) 849–857.